Ultrasonic anemometer angle of attack errors under turbulent conditions

Taro Nakai [a,*], Kou Shimoyama [b]

[a] International Arctic Research Center, University of Alaska Fairbanks, 930 Koyukuk Drive, Fairbanks, AK 99775-7340, USA
[b] Institute of Low Temperature Science, Hokkaido University, N19 W8, Kita-Ku, Sapporo 060-0819, Japan

ARTICLE INFO

ABSTRACT

Measurements of eddy fluxes are premised on the assumption that wind velocities are measured accurately by an ultrasonic anemometer. Recently, Gill ultrasonic anemometers have been shown to suffer errors depending on the angle of attack, which is the angle between the wind vector and the horizontal. The correction of these errors results in general eddy flux increases. However, since calibration for error dependent on angle of attack was carried out in a wind tunnel experiment under conditions of nearly laminar flow, the applicability of this correction to the field data under turbulent conditions has been questioned. In this study, angle of attack errors from a Gill WindMaster ultrasonic anemometer were assessed by field experiment, over meadow and under turbulent conditions. By using five identical anemometers, two configurations were evaluated: two pairs of anemometers for reference and one between the pairs for tilt. The dependence of anemometer (co)sine response on 0 to −90° angles of attack in 10° steps and at 45° were checked. It was clarified that errors dependent on angle of attack occur even under turbulent conditions, with results similar to the wind tunnel experiments. Sine responses of vertical wind velocities here depended not only on vertical angle of attack but also on horizontal wind direction, a dynamic not considered in previous studies. For a more robust correction, alternative calibration functions were obtained empirically, so as to reasonably explain our field experimental results. Applying this new correction, eddy fluxes increased substantially even over meadow, which is somewhat aerodynamically smooth compared with forests or agricultural fields.

1. Introduction

The eddy covariance technique is a commonly employed method for evaluating the fluxes of sensible heat, latent heat, and carbon dioxide. Measurements of eddy fluxes using this technique are premised on the assumption that wind velocities are measured accurately by an ultrasonic anemometer. However, in recent years, ultrasonic anemometers have been shown to suffer errors due to the angle of attack, which is the angle between the wind vector and the horizontal. Gash and Dolman (2003) first suggested the possibility of this error issue by concluding that a large proportion of daytime fluxes (about 20% over short vegetation and about 50% over forest) were carried by eddies with angles of attack outside the manufacturer's operating envelope of ±20° (R3-50 and WindMaster Pro, Gill Instruments, Lymington, UK), in spite of the fact that the frequency of occurrence of such large angles was relatively low. Actual calibration of these types of anemometers (i.e., Solent R2- and R3-type anemometers, Gill Instruments) was carried out by van der Molen et al. (2004), by means of a wind tunnel. They

confirmed that the sine response (i.e., the vertical wind velocity component) was substantially underestimated by anemometers, especially at a large angle of attack, and the cosine response (i.e., the horizontal velocity component) was also skewed with respect to the angle of attack and the wind direction. By using these calibration results, van der Molen et al. (2004) provided a method for correcting these ultrasonic anemometer errors. Building on the work of van der Molen et al. (2004), Nakai et al. (2006) proposed an improved method that gives a closer representation of their wind tunnel calibration data. Since the observed wind data contains error, the angle of attack calculated from the observed wind data is 'false', and the 'true' angle of attack should be calculated from the corrected or 'true' wind data. To solve this problem, Nakai et al. (2006) provided a method for deriving a 'true' (without error) angle of attack from the observed (error-containing) wind data, by solving a nonlinear equation that connects the 'false' angle of attack to the 'true' one. By using the obtained 'true' angle of attack, Nakai et al. (2006) achieved a more accurate correction than that of van der Molen et al. (2004). This error correction results in general increases in eddy fluxes (van der Molen et al., 2004; Nakai et al., 2006), and such increases in fluxes are considered to account for a large portion of energy imbalance (Nakai et al., 2006). Cava et al. (2008) analyzed energy balance closure over short vegetation, and pointed out that the correction of angle of attack dependent errors improved global (long-term)

* Corresponding author. Tel.: +1 907 474 7254; fax: +1 907 474 2691.
E-mail addresses: tnakai@iarc.uaf.edu, taro.nakai@gmail.com (T. Nakai).
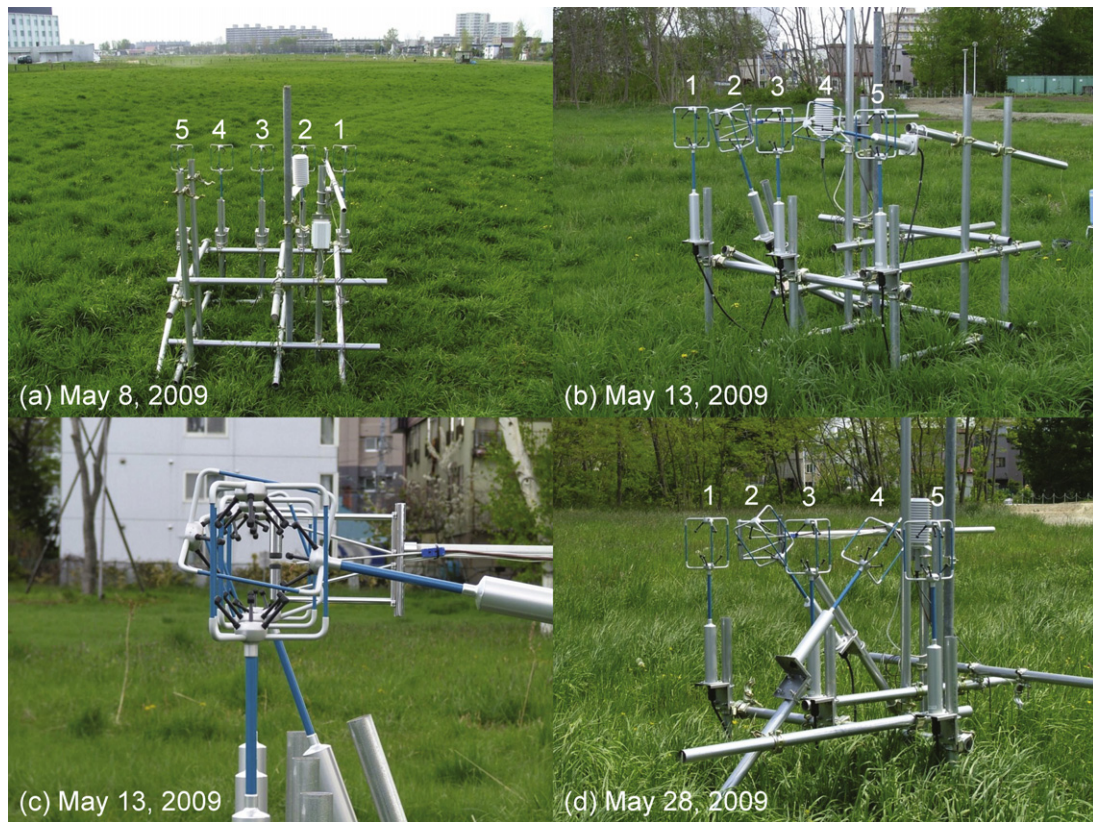URL: http://sites.google.com/site/micrometeorologist/ (T. Nakai).

Fig. 1. Photographs of experimental designs. (a) Instrument arrangement for cross checking ($\alpha_{t,2} = \alpha_{t,4} = 0°$) on upwind grassland; (b) angle of attack dependent calibration for $\alpha_{t,2} = -20°$ and $\alpha_{t,4} = -80°$; (c) side view of (b); (d) experimental condition when $\alpha_{t,2} = -40°$ and $\alpha_{t,4} = +45°$.

energy balance, though the effect of this correction on the daily variation of the 'short-term' energy residual was not significant.

On the other hand, some have questioned the application of wind tunnel derived corrections to field data. Such questions are based on the suggestions of Högström and Smedman (2004) that calibration results obtained in a wind tunnel, considered to be 'under nearly laminar flow condition', do not work satisfactorily in a natural turbulent flow. Following such studies, Foken (2008) concluded that the effect of angle of attack errors on the energy balance closure problem is less significant, though he recognized the possibility of the influence of this error. However, Högström and Smedman (2004) did not consider the effect of the angle of attack as examined by van der Molen et al. (2004). In addition, Meyers and Heuer (2006) reported that angle of attack errors were confirmed under turbulent conditions by field observations over a forest, using Model 81000 ultrasonic anemometers (R.M. Young, Traverse, Michigan, USA). This suggests that these errors can occur even under turbulent conditions, and not only when using Gill ultrasonic anemometers but also anemometers of other manufacturers. Importantly, though, angle of attack errors under turbulent conditions have not been examined systematically so far, and so both the occurrence of angle of attack errors in the natural turbulent flow and the applicability of the calibration results by van der Molen et al. (2004) under such conditions are still unclear. Since uncertainties in available energy (net radiation and soil heat flux) have been reported not to account for the lack of the energy balance closure (Twine et al., 2000), the uncertainty in measuring eddy covariance fluxes should be clarified to explain the energy imbalance problem. This would also directly affect the measure of trace gas fluxes.

The aim of this study was to clarify the issue of ultrasonic anemometer angle of attack errors in the natural turbulent flow.

2. Method

A field experiment for calibration was carried out from May 1 to June 5, 2009, over a meadow at Hokkaido University, Japan (43°05′03″N, 141°20′15″E). This meadow was originally a pure stand of orchard grass (*Dactylis glomerata*), but it is now mixed with weedy grasses. The mean plant height of these grasses was about 10 cm or less at the beginning of this study, and they grew up to about 100 cm (orchard grass) and 30 cm (weedy grasses) by the end of the observation period.

Fig. 1 shows the experimental design of this study. Five Wind-Master ultrasonic anemometers (Gill Instruments, Lymington, UK) were used in this calibration. This anemometer is identical in physical shape to the ones that van der Molen et al. (2004) calibrated in their wind tunnel experiment. Hereafter, these five ultrasonic anemometers are referred to as SAT1–SAT5 (these labels are shown in Fig. 1(a)). The anemometers were aligned perpendicularly to the direction with the longest fetch of meadow (ca. 120 m). Fig. 2 shows the definition of the coordinate system of the horizontal wind components u (m s^{-1}) and v (m s^{-1}), and the vertical component w (m s^{-1}) of the WindMaster anemometer. The north spar (or 'north marker') of the WindMaster was set to the opposite direction, and the horizontal rotation was fixed; thus, the wind direction of this longest-fetch direction is 'south' or 180° from the north in the coordinate system of the WindMaster (Fig. 2). The directions of these anemometers were determined carefully by eye. The height of the center of the measuring path of these anemometers was set at 1.35 m from the ground, and the spacing of each anemometer was 0.5 m. By using five identical anemometers, two pairs of systems were prepared: a pair of anemometers on each side for reference and one between them for tilt, as shown in Fig. 1(b). The preset tilt angle $\alpha_{t,i}$ (°) ($i = 1, \ldots, 5$) and the observation periods for
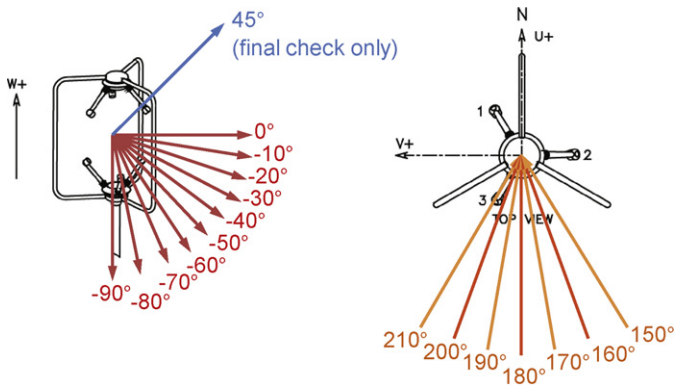
Fig. 2. Schematic diagram of the coordinate system of the WindMaster ultrasonic anemometer, together with the preset tilt angle $\alpha_{t,k}$ and wind direction γ_k taken into account in this study.
From Gill Instruments Ltd., 2009, edited.

SAT1–SAT5 are listed in Table 1. The tilt angles of the anemometers were checked by angle meter (slant level, read by eye; representational accuracy is $1°$). Note that the tilt angles of the anemometers were determined relative to a horizontal plane normal to the direction of gravity, not the angle relative to the ground surface.

This system was designed for wind from one side direction—i.e., from left to right in Fig. 1(c). In this design, (co)sine response can be checked for $-90° \le \alpha_{t,k} \le 0°$ ($k = 2, 4$) only, because the reference wind speeds of SAT1, 3, and 5 can be affected by the mounting structure of the tilted SAT2 and/or SAT4 when $0° < \alpha_{t,k} \le 90°$, as in Fig. 1(d). Therefore, the calibration was conducted for the angle of attack range of $-90° \le \alpha_{t,k} \le 0°$, and the observed results of $\alpha_{t,k} = 45°$ were used for validation of the newly determined calibration functions at the positive angle of attack, even though a single positive angle of attack limits validation of functions for the range of $0° < \alpha_{t,k} \le 90°$. Here it should be noted that errors were determined for $w < 0$ only, assuming that the results for $w > 0$ are symmetrical, depending on the position of the transducers (see Section 3.4).

Three-dimensional velocity components and sonic temperature were sampled at 10 Hz. In this study, 'Instantaneous Sampling' was 'Off'—i.e., each 10 Hz data entry was the average of 20 Hz raw data; and the 'on-board calibration' was 'Enabled' (Gill Instruments Ltd., 2009). The combination of these settings is considered commonly employed at most flux study sites, and so the calibration results in this study, with these settings, would be immediately applicable to the observed results of such study sites. In addition, variation of water vapor was also measured by KH-20 krypton hygrometer (Campbell Scientific, Logan, UT, USA) at 10 Hz, to assess the effect of the correction of angle of attack error on the latent heat flux. These data were logged in a CR5000 data logger (Campbell Scientific, Logan, UT, USA).

For each instance of 10-Hz wind data $\mathbf{U}_i = (u_i, v_i, w_i)$ ($i = 1, \ldots, 5$), observed instantaneous SAT2 and SAT4 sine and cosine responses,

S_k and C_k ($k = 2, 4$), and SAT1–5 angle of attack α_i and wind direction γ_i were calculated as follows.

$$S_k = \frac{w_k}{(|\mathbf{U}_{k-1}| + |\mathbf{U}_{k+1}|)/2} \quad (k = 2, 4), \tag{1}$$

$$C_k = \frac{\sqrt{u_k^2 + v_k^2}}{(|\mathbf{U}_{k-1}| + |\mathbf{U}_{k+1}|)/2} \quad (k = 2, 4), \tag{2}$$

$$\alpha_i = \arctan \frac{w_i}{\sqrt{u_i^2 + v_i^2}}, \tag{3}$$

$$\gamma_i = 180 - \arctan \frac{v_i}{u_i}, \tag{4}$$

where $|\mathbf{U}_i| = \sqrt{u_i^2 + v_i^2 + w_i^2}$ (m s^{-1}). If there is no error in measurements, S_i and C_i are equivalent to $\sin \alpha_i$ and $\cos \alpha_i$, respectively. Note that wind direction γ_i is not the actual azimuth direction, but the one defined by the WindMaster coordinate system.

In this study, horizontal wind speeds of SAT1, 3, and 5 were used as references, under the assumption that wind speeds with a small angle of attack are measured correctly by the WindMaster. Therefore, the data set within the criteria $|\tan \alpha_{k\pm1}| < 0.01$ (or $|\alpha_{k\pm1}| < 0.57°$); $||\mathbf{U}_{k-1}| - |\mathbf{U}_{k+1}|| < 0.05$ (m s^{-1}); and $2 < |\mathbf{U}_{k-1}| < 5$ (m s^{-1}) ($k = 2, 4$) were picked up.

To consider the angle of attack errors with respect to wind direction, wind direction of $\gamma_k = 150–210°$ ($k = 2, 4$) was taken into account in $10°$ steps (see Section 3.4). The data were binned into $\pm5°$ at each $10°$ interval, and the arithmetic mean value of each bin was used for calibration. Since this wind direction is defined on the 'tilted' $u_k v_k$ plane of SAT2 and 4, the angle between wind vector and $u_k v_k$ plane α'_k is different from the preset angle $\alpha_{t,k}$, and is calculated as follows (see Appendix B).

$$\alpha'_k = \arctan(-\cos \gamma_k \cdot \tan \alpha_{t,k}). \tag{5}$$

Note that binning with respect to the wind direction was done for all instantaneous wind data sets of $\mathbf{U}_{k-1}$, $\mathbf{U}_k$, and $\mathbf{U}_{k+1}$ ($k = 2, 4$) at each preset tilt angle $\alpha_{t,k}$.

3. Results and discussion

3.1. Reliability of the experimental design

As a preliminary observation, the reliability of this study's experimental design was checked by using SAT1–5 without tilting, as shown in Fig. 1(a). First, by using 1-min-average data of u_i and v_i, the relative difference in wind direction γ_i was checked. Since the directions of SAT1–5 were checked by eye, relative differences in γ_i had a bias. Bias of γ_i was $-2.60°$ (SAT1), $-0.42°$ (SAT2), $1.96°$ (SAT3), $0.75°$ (SAT4), and $0.31°$ (SAT5) on average, and the relative difference of γ_i was $4.56°$ at maximum, though these differences were unavoidable. Nevertheless, these deviations do not affect calibrations in this study. In addition, even considering these deviations of wind direction, other characteristics of air flow, such as flow around the equipment, were not confirmed by observation.

Next, the data selection procedure explained in Section 2 was tested for untilted anemometers. The difference between wind speed $|\mathbf{U}_k|$ and reference wind speed $(|\mathbf{U}_{k+1}| + |\mathbf{U}_{k-1}|)/2$ ($k = 2, 4$) of SAT2 and SAT4 were both -0.02 ± 0.13 m s^{-1} in average $\pm$ standard deviation, irrespective of the wind speed. On the other hand, SAT2 and SAT4 angles of attack α_k were $\alpha_2 = -0.56 \pm 1.57°$ and $\alpha_4 = 0.39 \pm 1.57°$, respectively. Though α_2 and α_4 showed some deviation from zero, it was smaller than the range of $\pm1°$, and was within the accuracy of reading the clinometer by eye. Considering the accuracy of measurement, therefore, the experimental design and the data selection method employed in this study should be acceptable.

Table 1
Observation period and the tilt angles $\alpha_{t,i}$ of ultrasonic anemometers SAT1–5.

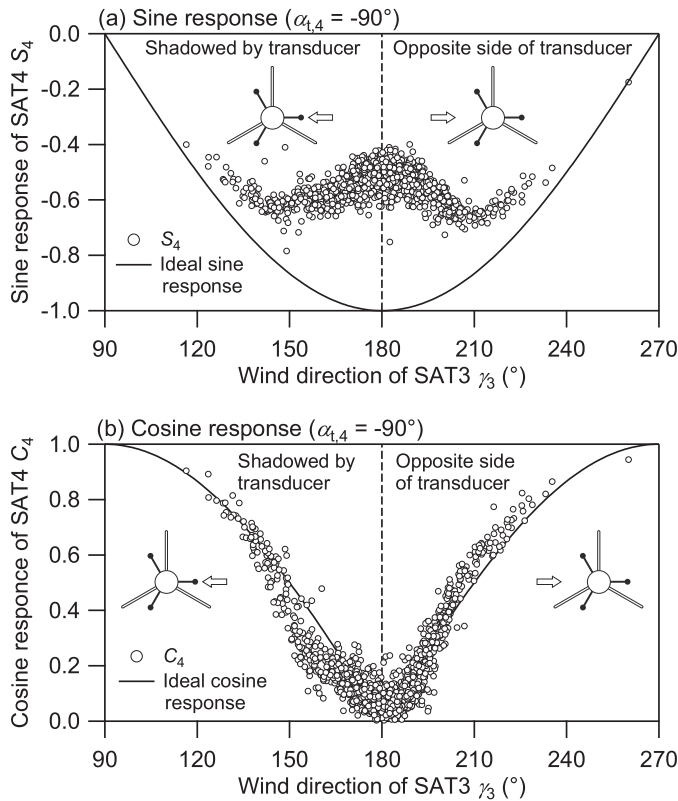| Period	SAT1 $\alpha_{t,1}$ (°)	SAT2 $\alpha_{t,2}$ (°)	SAT3 $\alpha_{t,3}$ (°)	SAT4 $\alpha_{t,4}$ (°)	SAT5 $\alpha_{t,5}$ (°)
May 1–9, 2009	0	0	0	0	0
May 9–10, 2009	0	−10	0	−90	0
May 10–12, 2009	0	−20	0	−90	0
May 13–15, 2009	0	−20	0	−80	0
May 15–20, 2009	0	−30	0	−70	0
May 20–24, 2009	0	−50	0	−60	0
May 24–25, 2009	0	−40	0	−60	0
May 25–28, 2009	0	−40	0	–	0
May 28–June 5, 2009	0	−40	0	+45	0

Fig. 3. Observed results of (a) sine response S_4 and (b) cosine response C_4 of SAT4 when the tilt angle was $\alpha_{t,4} = -90°$. The wind direction of $\gamma_3 = 180°$ corresponds to the angle of attack of $\alpha = -90°$ for SAT4. Schematics in the plots are the top view of the WindMaster ultrasonic anemometer with the upper transducers; these describe the relationship between the wind direction ($\gamma_3 < 180°$, $\gamma_3 > 180°$) and the position of the upper transducers.

3.2. (Co)sine response results when $\alpha_{t,4} = -90°$

When the tilt angle of SAT4 is set to $\alpha_{t,4} = -90°$, variation in the wind direction of SAT3 γ_3 can be converted to the variation in the angle of attack α for SAT4—i.e., $\gamma_3 \leq 180°$ represents $\alpha = 90° - \gamma_3$, at which air flow is shadowed by the transducer, and $\gamma_3 \geq 180°$ represents $\alpha = \gamma_3 - 270°$, at which air flows from the opposite side of the transducer ($\gamma_3 = 180°$ corresponds to $\alpha = -90°$). Therefore, the ideal sine responses are represented as $\sin(90° - \gamma_3)$ for $\gamma_3 \leq 180°$ and $\sin(\gamma_3 - 270°)$ for $\gamma_3 \geq 180°$, and similarly, the ideal cosine response is represented as $\cos(90° - \gamma_3)$ for $\gamma_3 \leq 180°$ and $\cos(\gamma_3 - 270°)$ for $\gamma_3 \geq 180°$. In this case, all observed data of S_4 and C_4 can be plotted against γ_3 and compared with the ideal sine and cosine responses.

Fig. 3 shows the observed results of sine response S_4 (Fig. 3(a)) and cosine response C_4 (Fig. 3(b)) of SAT4. Obviously, S_4 was underestimated around $\gamma_3 = 180°$, and the shape of this response was similar to the wind tunnel results by van der Molen et al. (2004). C_4 also deviated from the ideal cosine response as presented by van der Molen et al. (2004)—it was under-measured when the wind was shadowed by the transducer ($\gamma_3 < 180°$) and over-measured when the wind flowed from the opposite side of the transducer ($\gamma_3 > 180°$), as pointed out by Nakai et al. (2006). These results clearly demonstrate that the angle of attack errors of the ultrasonic anemometer occur even under turbulent conditions, and the errors occur not randomly but systematically, depending on the angle of attack. In addition, both C_4 and S_4 were asymmetric with respect to $\gamma_3 = 180°$, indicating that S_4 was also affected by the presence or absence of transducer shadowing, depending on the wind direction.
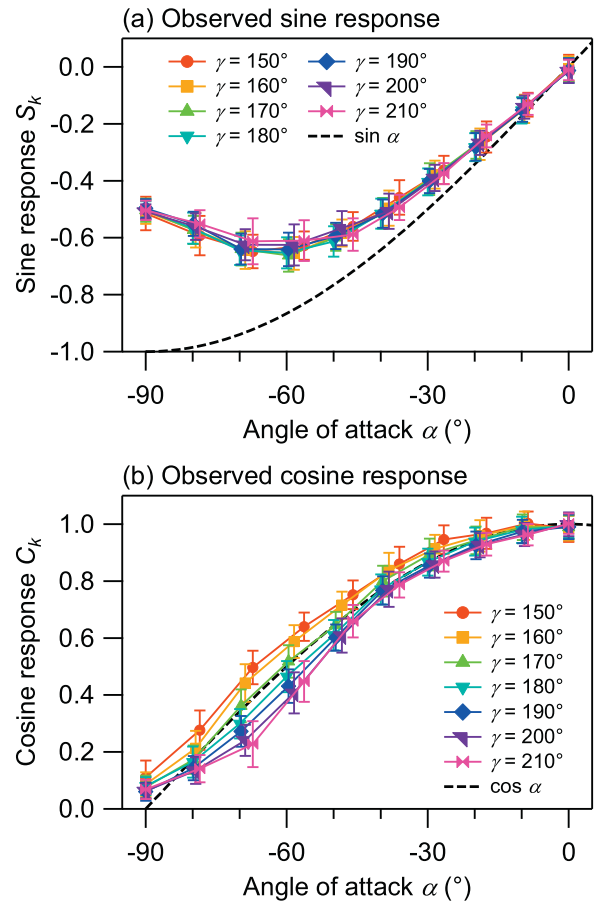

Fig. 4. Observed angle of attack dependency of (a) sine response S_k and (b) cosine response C_k with respect to wind direction. The angle of attack of each wind direction data is α'_k calculated from Eq. (5). Markers and errorbars indicate the average and standard deviation, respectively.

3.3. (Co)sine response under turbulent conditions

Hereafter, the actual angles of attack for SAT2 and SAT4 α'_k ($k = 2$, 4), defined by the wind direction γ_k and tilt angle $\alpha_{t,k}$ (see Section 2, Appendix B), is represented by the angle of attack α (°), and the wind direction of SAT2 and SAT4 γ_k ($k = 2, 4$) on the 'tilted' $u_k v_k$ plane is represented by the wind direction γ (°).

Fig. 4 shows the observed angle of attack dependency of sine response S_k (Fig. 4(a)) and cosine response C_k (Fig. 4(b)), with respect to wind direction γ. Clearly, both S_k and C_k showed angle of attack dependent errors. The characteristics of these errors are similar to those of the wind tunnel experiments of van der Molen et al. (2004), in that the underestimation of S_k was greater at a larger angle of attack, and the shape of C_k varied with wind direction.

However, the calibration functions undertaken by Nakai et al. (2006) (i.e., calibration results of van der Molen et al., 2004) and the field observation results in this study were somewhat different. Fig. 5 shows the wind speed ratio $r_{U,k} = 2|\mathbf{U}_k|/(|\mathbf{U}_{k-1}| + |\mathbf{U}_{k+1}|)$ (Fig. 5(a)), cosine response C_k (Fig. 5(b)), and sine response S_k ($k = 2, 4$) (Fig. 5(c)), with respect to the angle of attack α before and after the application of the correction of Nakai et al. (2006) for the wind direction $\gamma = 180°$. In the case of the sine response, the observed results of S_k in this study (filled circles in Fig. 5(c)) showed a smoother transition with respect to the angle of attack α, compared to the sine response function $f_{sr}(\alpha)$ (Eq. (7) by Nakai et al., 2006). The observed C_k in this study and the cosine response function $f_{cr}(\alpha, \gamma)$ (Eq. (10) by Nakai et al., 2006) were also different (Fig. 5(b)). These differences may result from a difference in
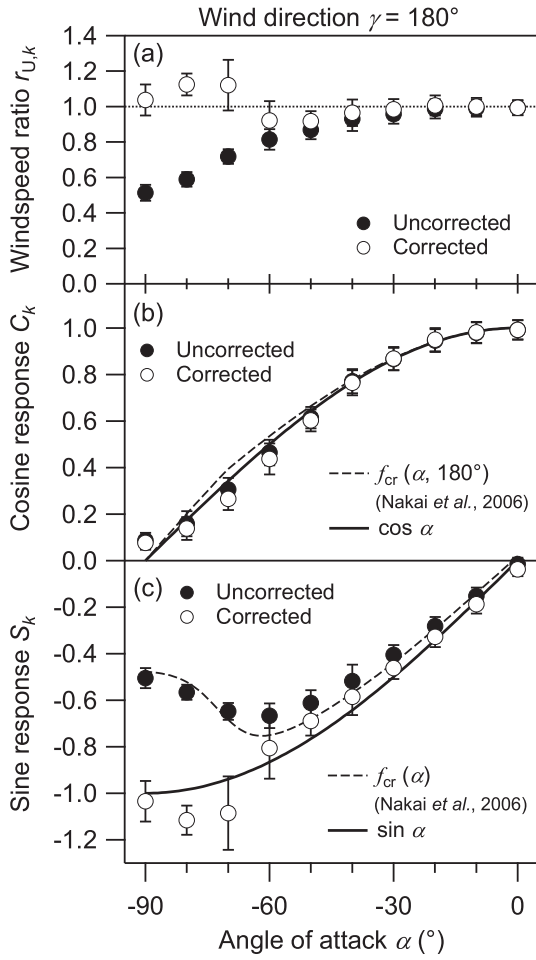
Fig. 5. (a) Wind speed ratio $r_{U,k} = 2|\mathbf{U}_k|/(|\mathbf{U}_{k-1}| + |\mathbf{U}_{k+1}|)$, (b) cosine response C_k, and (c) sine response S_k ($k = 2, 4$) with respect to angle of attack α before and after the application of the Nakai et al. (2006) correction for the wind direction $\gamma = 180°$. (Co)sine response functions and (co)sine functions are also plotted. The angle of attack of each observed data is α'_k, calculated from Eq. (5). Markers and errorbars indicate the average and standard deviation, respectively.

observation conditions—i.e., the wind tunnel experiment's nearly laminar flow (van der Molen et al., 2004; Nakai et al., 2006) and this study's field experiment under turbulent conditions. Due to the discrepancy between the observed results in this study and the calibration functions by Nakai et al. (2006), the corrected results of S_k and C_k by Nakai et al. (2006) (open circles in Fig. 5(b) and (c)) largely deviated from the sine and cosine functions, respectively. The wind speed ratio $r_{U,k}$, calculated as the result of the correction by Nakai et al. (2006), also deviated largely from unity (Fig. 5(a)). For a more robust correction, alternative calibration functions are required.

3.4. New calibration functions

In this section, new calibration functions are introduced in order to represent the observed results in this study properly. The observed vertical wind velocity w_o and horizontal wind speed $U_o (= \sqrt{u_o^2 + v_o^2})$ are converted into the 'true' vertical wind velocity w and horizontal wind speed $U (= \sqrt{u^2 + v^2})$ by the following equations.

$$w = w_o \frac{\sin \alpha}{f_{sr}(\alpha, \gamma)}, \tag{6}$$

$$U = U_o \frac{\cos \alpha}{f_{cr}(\alpha, \gamma)}, \tag{7}$$

where $f_{sr}(\alpha, \gamma)$ is the sine response function and $f_{cr}(\alpha, \gamma)$ is the cosine response function. These functions were designed to describe the observed sine response S_k and cosine response C_k, respectively.

The sine and cosine response functions can take arbitrary shapes, as in van der Molen et al. (2004) and Nakai et al. (2006). In this study, $f_{sr}(\alpha, \gamma)$ and $f_{cr}(\alpha, \gamma)$ are defined as

$$f_{sr}(\alpha, \gamma) = \phi_{sr}(\alpha, \gamma) \sin \alpha, \tag{8}$$

$$f_{cr}(\alpha, \gamma) = \phi_{cr}(\alpha, \gamma) \cos \alpha, \tag{9}$$

where $\phi_{sr}(\alpha, \gamma)$ and $\phi_{cr}(\alpha, \gamma)$ are the correction functions for the sine and cosine responses, respectively. After defining $f_{sr}(\alpha, \gamma)$ and $f_{cr}(\alpha, \gamma)$ (in Eqs. (8) and (9), respectively) the correction functions $\phi_{sr}(\alpha, \gamma)$ and $\phi_{cr}(\alpha, \gamma)$ are defined from Eqs. (6) and (7) as

$$\phi_{sr}(\alpha, \gamma) = \frac{f_{sr}(\alpha, \gamma)}{\sin \alpha} = \frac{w_o}{w}, \tag{10}$$

$$\phi_{cr}(\alpha, \gamma) = \frac{f_{cr}(\alpha, \gamma)}{\cos \alpha} = \frac{U_o}{U}. \tag{11}$$

Therefore, $\phi_{sr}(\alpha, \gamma)$ and $\phi_{cr}(\alpha, \gamma)$ represent how w and U are affected by the errors depending on the angle of attack α and wind direction γ. Note that, since $f_{sr}(\alpha, \gamma)$ and $f_{cr}(\alpha, \gamma)$ represent the observed sine response S_k and cosine response C_k, respectively, the correction functions $\phi_{sr}(\alpha, \gamma)$ and $\phi_{cr}(\alpha, \gamma)$ represent the observed $S_k/\sin \alpha$ and $C_k/\cos \alpha$, respectively.

As described in Section 2, the calibrations were made in the range $-90° \leq \alpha \leq 0°$ only. For $\alpha \leq 0°$, considering the observed fact that both the sine and cosine responses varied not only with angle of attack but also with wind direction (see Section 3.3), $\phi_{sr}(\alpha, \gamma)$ and $\phi_{cr}(\alpha, \gamma)$ are described as follows.

$$\phi_{sr}(\alpha, \gamma) = A(\alpha) - B(\alpha) \sin 3\gamma \quad (-90° \leq \alpha \leq 0°), \tag{12}$$

$$\phi_{cr}(\alpha, \gamma) = C(\alpha) + D(\alpha) \sin 3\gamma \quad (-70° \leq \alpha \leq 0°), \tag{13}$$

$$\phi_{cr}(\alpha, \gamma) = \phi_{cr}(-70°, \gamma) \quad (-90° \leq \alpha < -70°), \tag{14}$$

where $A(\alpha)$, $B(\alpha)$, $C(\alpha)$, and $D(\alpha)$ are the 5th-order polynomial functions of α and are defined as

$$A(\alpha) = a_1 \alpha^5 + a_2 \alpha^4 + a_3 \alpha^3 + a_4 \alpha^2 + a_5 \alpha + 1, \tag{15}$$

$$B(\alpha) = b_1 \alpha^5 + b_2 \alpha^4 + b_3 \alpha^3 + b_4 \alpha^2 + b_5 \alpha, \tag{16}$$

$$C(\alpha) = c_1 \alpha^5 + c_2 \alpha^4 + c_3 \alpha^3 + c_4 \alpha^2 + c_5 \alpha + 1, \tag{17}$$

$$D(\alpha) = d_1 \alpha^5 + d_2 \alpha^4 + d_3 \alpha^3 + d_4 \alpha^2 + d_5 \alpha, \tag{18}$$

where a_j, b_j, c_j, and d_j ($j = 1, \ldots, 5$) are coefficients. Note that both $\phi_{sr}(\alpha, \gamma)$ and $\phi_{cr}(\alpha, \gamma)$ are equal to unity when $\alpha = 0°$, based on the assumption that the wind velocity is measured by the WindMaster correctly at the small angle of attack α.

Here we note the relationship between wind direction and the structure of the WindMaster, and the function $\sin 3\gamma$ in Eqs. (12) and (13). Fig. 6 shows the positional relationship between parts of the WindMaster (i.e., support spars and transducers) and wind direction. Wind attacks the support spar when $\gamma = 0°$, 120°, and 240°. The lower transducer appears when $\gamma = 30°$, 150°, and 270°, and the upper transducer appears when $\gamma = 90°$, 210°, and 330°. Therefore, if the error is affected by the presence or absence of transducer shadowing, which depends on the wind direction (see Section 3.2), this effect may be expressed by the function of $\sin 3\gamma$ as shown in Fig. 6.

Fig. 7(a) shows the distribution of the angle of attack α (= α'_4), cosine response C_4, and ideal cosine response $\cos \alpha$ against wind direction γ ($90° \leq \gamma \leq 270°$), when the preset tilt angle was $\alpha_{t,4} = -60°$. Due to the experimental design (see Section 2), α
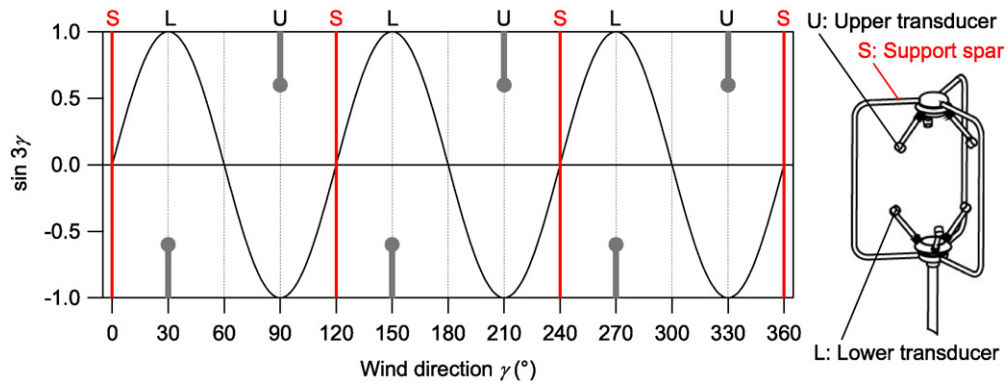
Fig. 6. Schematic diagram of the positional relationship of the WindMaster support spars and transducers, against the wind direction γ, together with the graph of $\sin 3\gamma$. In this figure, S, L, and U denote the direction of support spar, lower transducer, and upper transducer, respectively.

changed according to γ, and approached $0°$ when γ approached $90°$ or $270°$. The distribution of C_4 against γ was asymmetrical with respect to $\gamma = 180°$, and deviated somewhat from $\cos \alpha$ in the range of $120° \leq \gamma \leq 240°$. As a result, the behavior of $C_4/\cos \alpha$ with respect to γ showed the shape of $\sin 3\gamma$ within $120° \leq \gamma \leq 240°$ (Fig. 7(b)), as seen in Fig. 6, though $C_4/\cos \alpha$ in this figure was affected not only by γ, but also by α. This result may support the dependence of the correction functions on $\sin 3\gamma$, as in Eqs. (12) and (13). In addition, the results of $C_4/\cos \alpha$ at $\gamma = 120°, 240°$ (distorted by spar) and at $\gamma = 180°$ (no spar) were not significantly different. One possible reason for this is that the distortion effects of the wind speed by the support spar (Högström and Smedman, 2004) were adequately removed by the on-board software as confirmed by van der Molen et al. (2004), since the 'on-board calibration' of the Wind-Master was 'Enabled' in this study. Therefore, the limited range of $150° \leq \gamma \leq 210°$ was taken into account in this study, assuming the dependence of the correction functions upon $\sin 3\gamma$ and neglecting the effect of the support spars.

As for $\alpha > 0°$, in view of the fact that the six WindMaster transducers are arranged in point symmetry, the same functions

(12)–(18) are used, by substituting $-\alpha$ for α and $\gamma + 180°$ for γ. Since errors for $\alpha > 0°$ were not checked in this study other than the single point $\alpha = 45°$, this is a weakly supported assumption.

From Eqs. (10) and (11), and considering that $\tan \alpha = w/U$, the following relationship is derived.

$$\frac{w_o}{U_o} = \frac{f_{sr}(\alpha, \gamma)}{f_{cr}(\alpha, \gamma)} = \frac{\phi_{sr}(\alpha, \gamma)}{\phi_{cr}(\alpha, \gamma)} \tan \alpha, \tag{19}$$

which is the nonlinear equation relating the observed w_o and U_o to the 'true' angle of attack α. Since $w_o/U_o = \tan \alpha_o$, where α_o is the observed angle of attack, the nonlinear Eq. (19) connects the observed α_o to the true α. Eq. (19) can be rearranged as:

$$\alpha = \arctan \left(\frac{\phi_{cr}(\alpha, \gamma)}{\phi_{sr}(\alpha, \gamma)} \frac{w_o}{U_o} \right), \tag{20}$$

which can be solved with the Steffensen method (Nakai et al., 2006). Finally, the corrected (or 'true') α can be derived from observed U_o and w_o by using the method of Nakai et al. (2006), with Eq. (20);
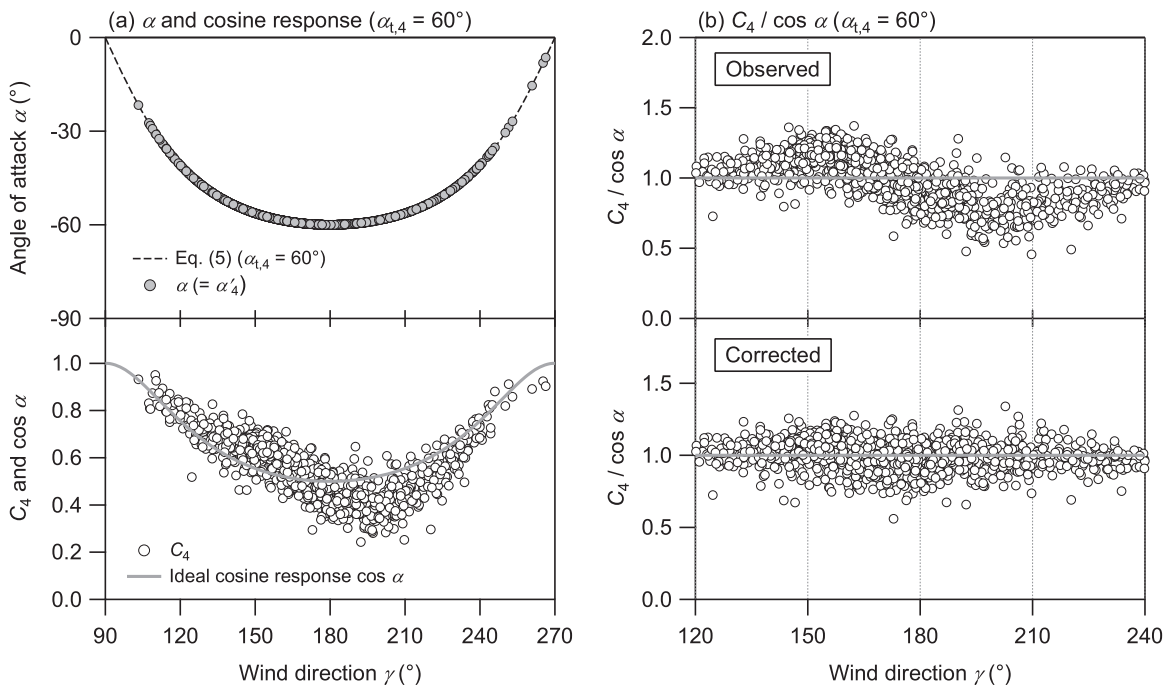

Fig. 7. Plots (a) of the distributions of the angle of attack $\alpha \ (= \alpha_4')$, cosine response C_4, and ideal cosine response $\cos \alpha$ against wind direction γ ($90° \leq \gamma \leq 270°$), and (b) the behavior of $C_4/\cos \alpha$ with respect to the wind direction γ ($120° \leq \gamma \leq 240°$), before and after the application of the new correction, when the preset tilt angle was $\alpha_{t,4} = -60°$.

the corrected u, v, and w are then obtained from the observed u_o, v_o, and w_o as follows, according to Eqs. (6)–(9).

$$u = \frac{u_o}{\phi_{cr}(\alpha, \gamma)}, \qquad (21)$$

$$v = \frac{v_o}{\phi_{cr}(\alpha, \gamma)}, \qquad (22)$$

$$w = \frac{w_o}{\phi_{sr}(\alpha, \gamma)}. \qquad (23)$$

Note that Eqs. (21) and (22) are based on the assumption that there is no significant error in the measured wind direction attributed to the angle of attack dependent error.

All the coefficients of $\phi_{sr}(\alpha, \gamma)$ and $\phi_{cr}(\alpha, \gamma)$ (i.e., Eqs. (15)–(18)) were determined by the least square method, against the experimental results (listed in Table 2). Fig. 8(a) and (b) shows the results of fitting $\phi_{sr}(\alpha, \gamma)$ and $\phi_{cr}(\alpha, \gamma)$ with their observations for the wind directions $\gamma = 150°$, $180°$, and $210°$. The finally obtained sine response function $f_{sr}(\alpha, \gamma)$ (Eq. (8)) and cosine response function $f_{cr}(\alpha, \gamma)$ (Eq. (9)) perform with α and γ as shown in Fig. 8(c) and (d), respectively.

Fig. 9 shows the wind speed ratio $r_{U,k}$, cosine response C_k, and sine response S_k ($k = 2, 4$), with respect to the angle of attack α before and after the application of the new corrections for $\gamma = 150°$ (Fig. 6(a)), $180°$ (Fig. 6(b)), and $210°$ (Fig. 6(c)). If not for angle of attack dependent errors, the wind speed ratio $r_{U,k}$ should be unity, irrespective of the angle of attack α. But in fact, $r_{U,k}$ was underestimated due to error, especially at a large α. Applying the correction of the newly proposed functions, $r_{U,k}$ was restored to unity successfully, even at a large α. Also, the uncorrected C_k and S_k were substantially represented by $f_{cr}(\alpha, \gamma)$ and $f_{sr}(\alpha, \gamma)$, and the corrected C_k and S_k were successfully restored to the $\cos \alpha$ and $\sin \alpha$, respectively.

Table 2
Coefficients of the polynomials $A(\alpha)$, $B(\alpha)$, $C(\alpha)$, and $D(\alpha)$ in the (co)sine response functions.

Polynomial	Coefficient	Value
$A(\alpha)$	a_1	-3.198×10^{-10}
	a_2	-2.698×10^{-8}
	a_3	4.167×10^{-6}
	a_4	4.853×10^{-4}
	a_5	1.674×10^{-2}
$B(\alpha)$	b_1	5.927×10^{-10}
	b_2	1.441×10^{-7}
	b_3	1.207×10^{-5}
	b_4	3.926×10^{-4}
	b_5	3.829×10^{-3}
$C(\alpha)$	c_1	-1.208×10^{-9}
	c_2	-1.581×10^{-7}
	c_3	-4.955×10^{-6}
	c_4	1.608×10^{-5}
	c_5	1.281×10^{-3}
$D(\alpha)$	d_1	2.272×10^{-9}
	d_2	3.856×10^{-7}
	d_3	2.034×10^{-5}
	d_4	3.942×10^{-4}
	d_5	9.184×10^{-4}

3.5. Validation of the correction with the new functions

3.5.1. 10-Hz raw data of the tilted anemometers

By rotating the coordinate system of SAT2 and SAT4, the 10-Hz raw data and their calculated sensible heat fluxes can be compared with those of the untilted reference anemometers. Each wind velocity component u_k, v_k, and w_k ($k = 2, 4$) of the tilted SAT2 and SAT4 can be rotated to the untilted (normal) coordination components
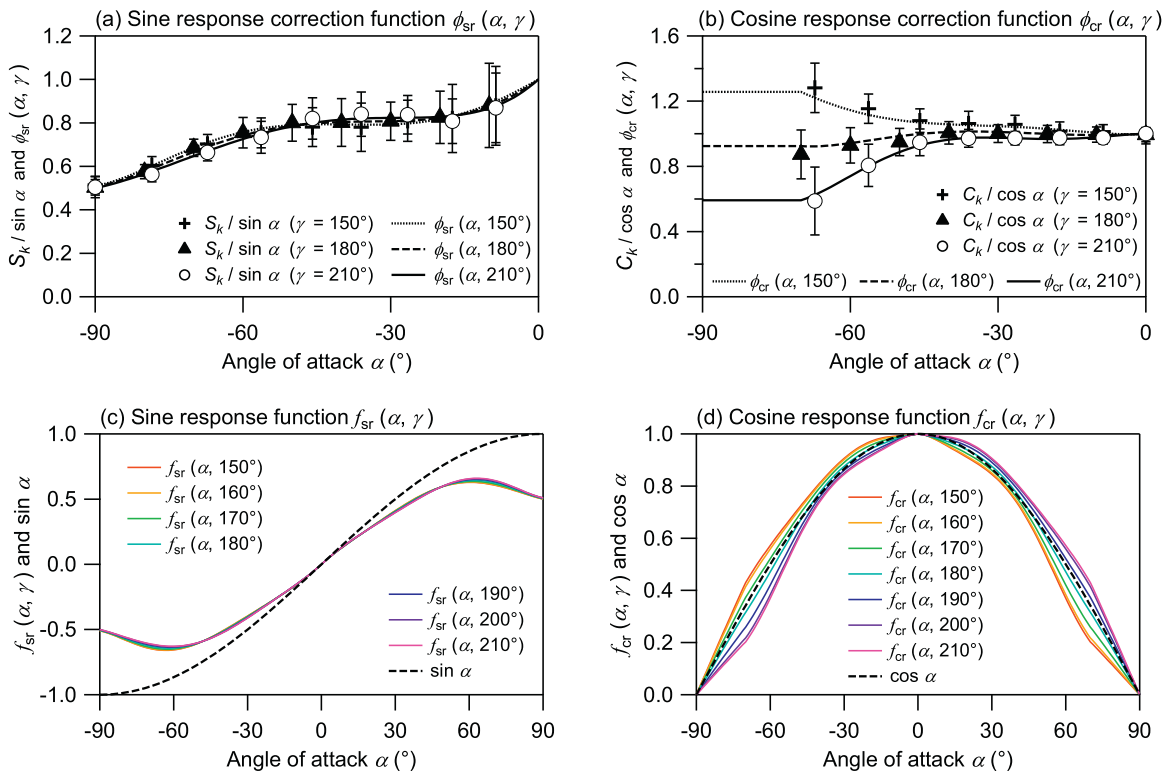

Fig. 8. Illustrative plots of the new correction functions. (a) Sine response correction function $\phi_{sr}(\alpha, \gamma)$ and corresponding observed values for the wind directions of $\gamma = 150°$, $180°$, and $270°$; (b) cosine response correction function $\phi_{cr}(\alpha, \gamma)$ and corresponding observations for $\gamma = 150°$, $180°$, and $270°$; (c) sine response function $f_{sr}(\alpha, \gamma)$; and (d) cosine response function $f_{cr}(\alpha, \gamma)$. The angle of attack for observed data in (a) and (b) is α_k', calculated from Eq. (5). Markers and errorbars in (a) and (b) indicate the average and standard deviation, respectively.
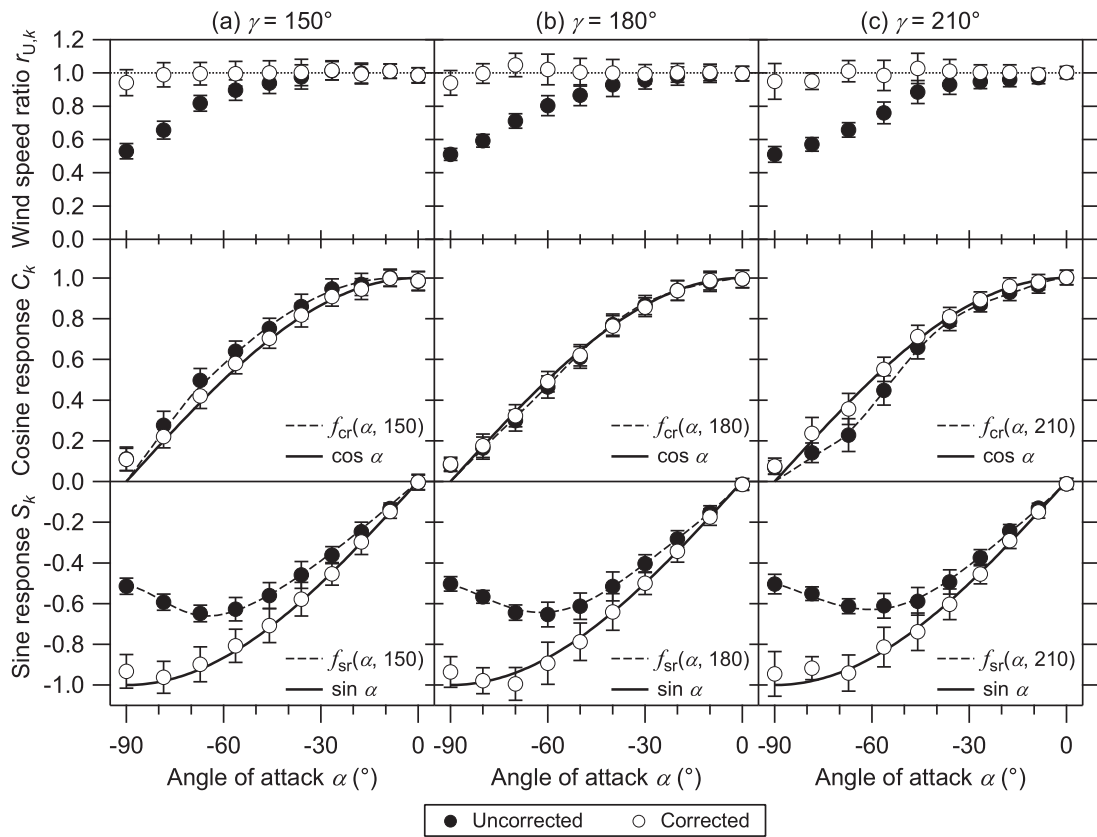
Fig. 9. Wind speed ratio $r_{U,k}$, cosine response C_k, and sine response S_k ($k = 2, 4$), with respect to angle of attack α before and after application of the new correction for (a) $\gamma = 150°$, (b) $180°$, and (c) $210°$. (Co)sine response functions and (co)sine functions are also plotted. The angle of attack for each observed data is α'_k, calculated from Eq. (5). Markers and errorbars indicate the average and standard deviation, respectively.

$u_{rot,k}$, $v_{rot,k}$, and $w_{rot,k}$ (m s^{-1}) with respect to the tilt angle $\alpha_{t,k}$ as follows.

$$u_{rot,k} = u_k \cos \alpha_{t,k} + w_k \sin \alpha_{t,k}, \tag{24}$$

$$v_{rot,k} = v_k, \tag{25}$$

$$w_{rot,k} = -u_k \sin \alpha_{t,k} + w_k \cos \alpha_{t,k}. \tag{26}$$

Fig. 10 shows the example of the 10-Hz raw data's temporal variation of w_1, $w_{rot,2}$ (Eq. (26)), and w_3, together with their frequency polygons, before and after the application of the new correction. Though the uncorrected $w_{rot,2}$ showed clear positive bias due to

the angle of attack dependent errors, the corrected $w_{rot,2}$ accorded well with w_1 and w_3, indicating that the application of the new correction to these data (SAT1, SAT2, and SAT3) was appropriate. Note that this is a special case of w_1 and w_3 as highly correlated, and they did not always correspond with one another. On the other hand, the peak of the frequency polygon of the observed $w_{rot,2}$ deviated from that of w_1 and w_3, and they were close to each other after the correction was applied (Fig. 10, right panel). Therefore, the closeness of the peak of the $w_{rot,k}$ frequency polygon with that of w_{k-1} and w_{k+1} is a good indicator that the correction is valid.
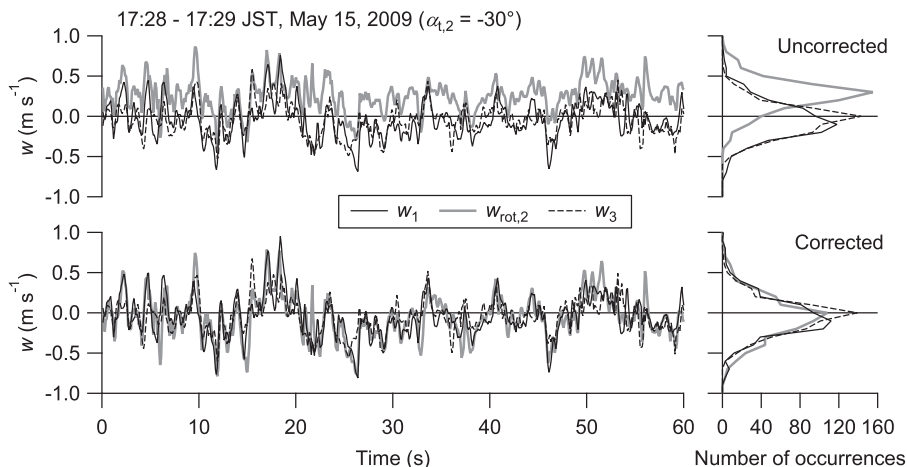

Fig. 10. An example of the temporal variation of w_1, $w_{rot,2}$ (Eq. (26)), and w_3 (left panel), and their frequency polygons with bin width of 0.1 m s^{-1} (right panel), before and after application of the new correction (17:28–17:29JST, May 19, 2009, tilt angle of SAT2 was $\alpha_{t,2} = -30°$).
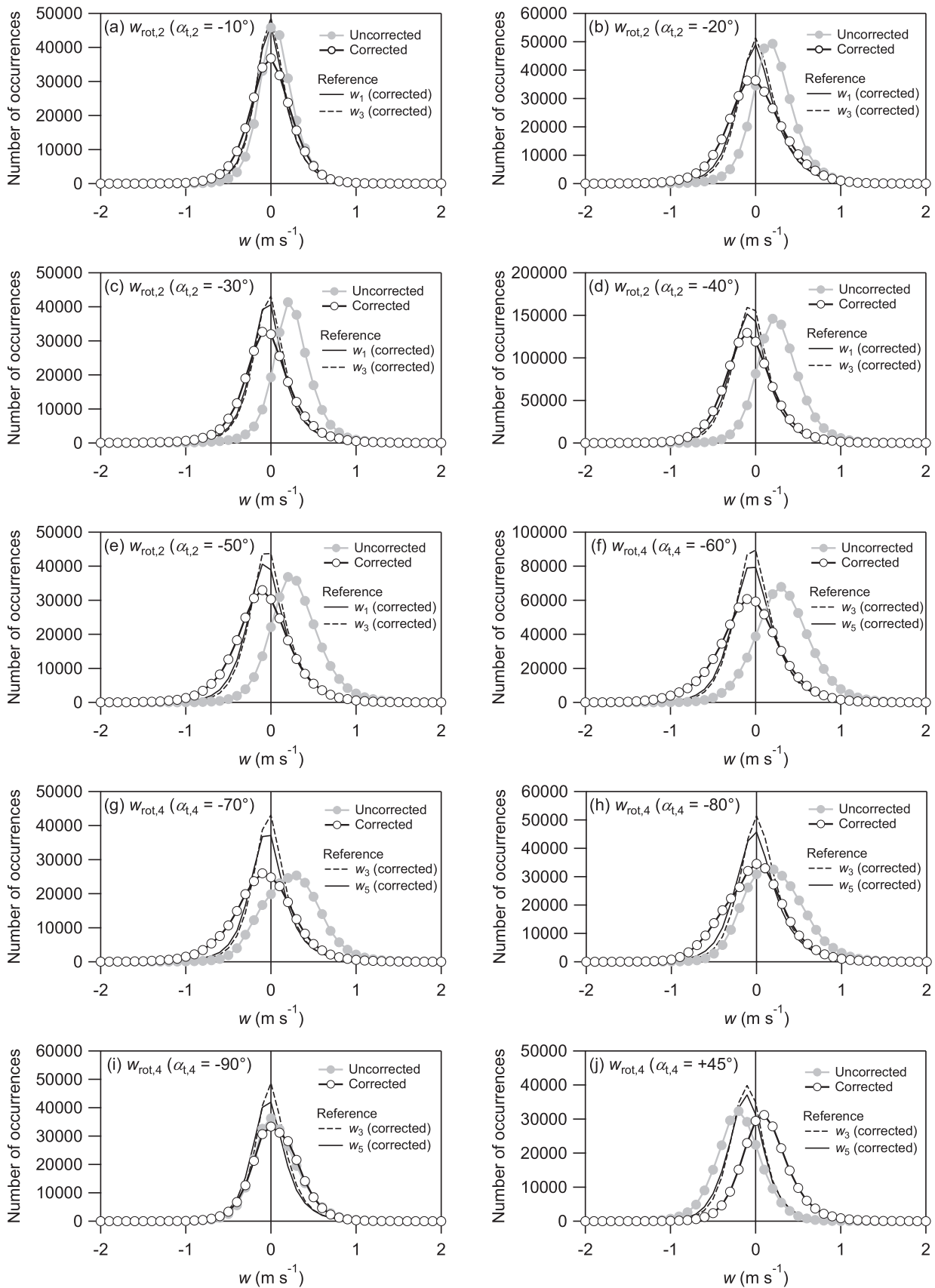
Fig. 11. Frequency polygons of $w_{rot,k}$ with bin width of 0.1 m s^{-1} for each tilt angle $\alpha_{t,k}$ (k = 2, 4), before and after application of the new correction, together with the corrected w_1, w_3, and w_5 as references. Each point on the graph corresponds to the center value of the bin. The data of $170° < \gamma_3 < 190°$ and $2 < |\mathbf{U}_3| < 5$ m s^{-1} were used.
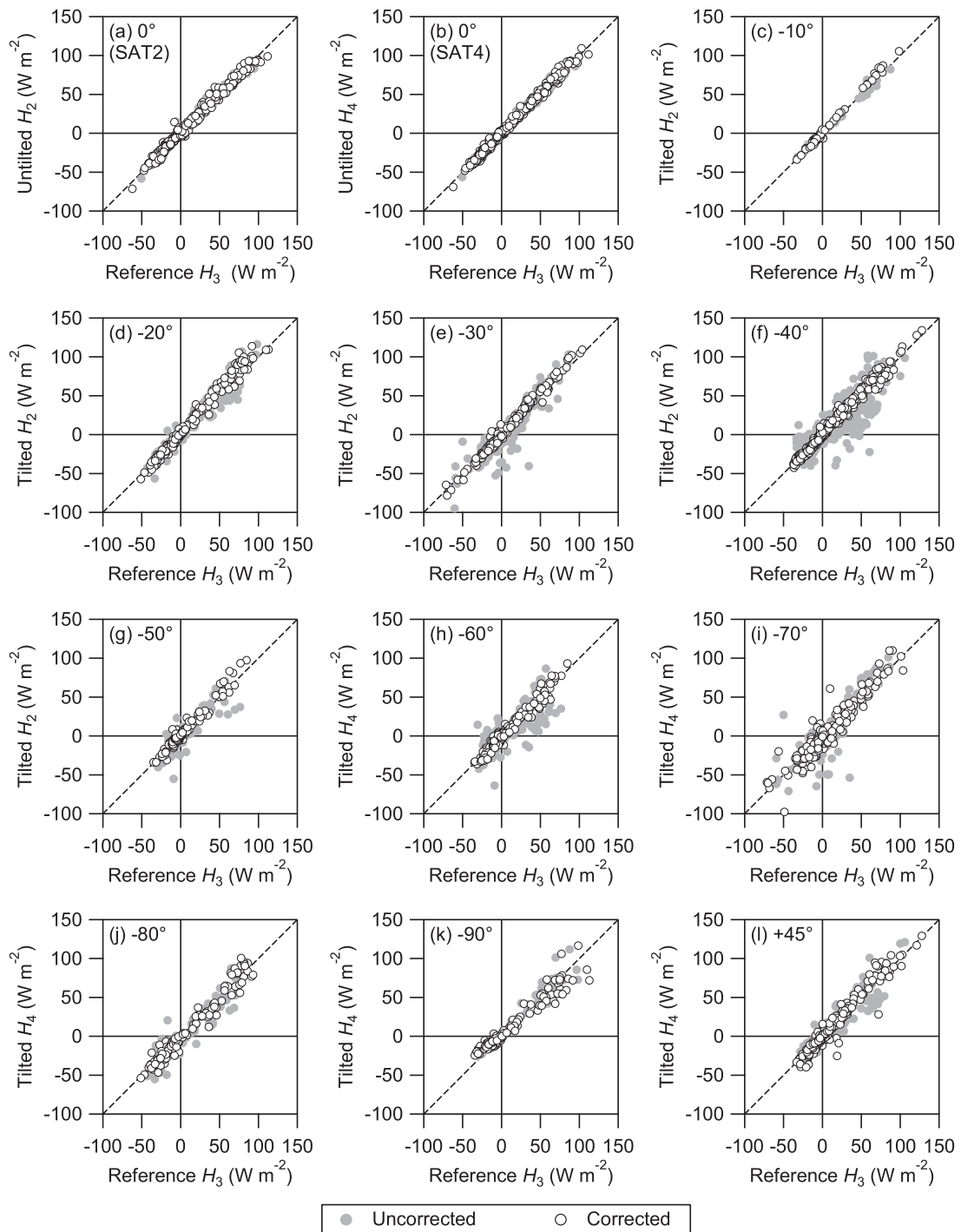
Fig. 12. Comparisons of sensible heat fluxes H between the reference ultrasonic anemometer SAT3 and the tilted anemometers SAT2 and SAT4 at each tilt angle, before and after application of the new correction.

Fig. 11 shows the frequency polygons of $w_{\mathrm{rot},k}$ for each tilt angle $\alpha_{\mathrm{t},k}$ ($k = 2, 4$), before and after the new correction was applied. The data of $170° < \gamma_3 < 190°$ and $2 < |\mathbf{U}_3| < 5\,\mathrm{m\,s^{-1}}$ were used. These data indicate that the uncorrected $w_{\mathrm{rot},k}$ was positively biased when $\alpha_{\mathrm{t},k} < 0°$ and negatively biased when $\alpha_{\mathrm{t},k} > 0°$. After the new correction was applied, the peak of the frequency polygon was close to that of w_{k-1} and w_{k+1} for each tilt angle when $\alpha_{\mathrm{t},k} < 0°$; thus, the application of the new correction to the 10-Hz raw data was considered valid for the data obtained under the conditions of $\alpha_{\mathrm{t},k} < 0°$.

However, the corrected results for the positive angle ($\alpha_{\mathrm{t},4} = 45°$) somewhat deviated from the peak of the w_3 and w_5 frequency polygon. A possible reason for this phenomenon is that the mounting structure of the tilted SAT4 may skew the airflow, and the angle of attack may became larger than horizontal. Therefore, the applicability of the new correction to the data of $\alpha_{\mathrm{t},4} = 45°$ could not be confirmed by this test. Validation for this data is discussed later, in Section 3.5.3.

3.5.2. Sensible heat fluxes of the tilted anemometers

Fig. 12 shows the scatter plots of the sensible heat flux H_k ($\mathrm{W\,m^{-2}}$) ($k = 2, 4$) of SAT2 and SAT4 against the reference sensible heat flux H_3 ($\mathrm{W\,m^{-2}}$) of SAT3, before and after the application

Table 3
The slope, intercept, and determination coefficient R^2 of the linear regression for the plots in Fig. 9, before and after the correction of this study was applied.

Plot	α_t	Uncorrected			Corrected		
		Slope	Intercept	R^2	Slope	Intercept	R^2
Fig. 9(a)	$0°$	0.981	0.717	0.986	0.981	0.786	0.987
Fig. 9(b)	$0°$	1.018	0.030	0.993	1.019	0.026	0.993
Fig. 9(c)	$-10°$	0.954	0.120	0.991	1.082	0.859	0.996
Fig. 9(d)	$-20°$	1.000	−0.229	0.940	1.104	1.758	0.985
Fig. 9(e)	$-30°$	1.001	−2.840	0.816	1.069	0.587	0.987
Fig. 9(f)	$-40°$	0.861	−0.804	0.729	1.054	0.118	0.986
Fig. 9(g)	$-50°$	0.972	−1.336	0.796	1.059	0.942	0.965
Fig. 9(h)	$-60°$	0.766	−1.480	0.619	1.030	−1.167	0.967
Fig. 9(i)	$-70°$	1.066	−4.185	0.774	1.015	−1.004	0.905
Fig. 9(j)	$-80°$	0.990	−3.558	0.908	1.021	−1.672	0.960
Fig. 9(k)	$-90°$	0.949	2.110	0.955	0.834	2.393	0.944
Fig. 9(l)	$+45°$	0.952	−0.126	0.897	1.076	−0.891	0.958

of the new angle of attack dependent error corrections. Note that both reference (untilted) anemometer SAT3 and objective (tilted) anemometers (SAT2 and SAT4) were corrected for the angle of attack dependent errors in the "corrected" plot. The horizontal coordinate rotations for $\overline{v_{\text{rot},k}} = 0$ ($k = 2, 4$) and $\overline{v_3} = 0$ (McMillen, 1988) were applied. Again, vertical coordinate rotation was made according to Eqs. (24) and (26), to restore the normal coordinate system from the data of the tilted anemometers. The sonic temperature of the WindMaster was corrected internally for crosswind, and only the humidity correction (Schotanus et al., 1983) was applied. The slope, intercept, and the determination coefficient R^2 of the linear regression for the plots in Fig. 12 are listed in Table 3.

After the new correction was applied, H of the 'tilted' anemometer agreed well with that of the 'untilted' reference SAT3 at each tilt angle, and the correlation between the two was significantly improved. If the new calibration functions and the method of correction were inadequate, the regression of this H would not be improved. Therefore, these results strongly support the validity of the new correction functions proposed in this study, and they ensure that the application of the correction of the angle of attack dependent errors to the 10-Hz raw data was appropriate.

3.5.3. Validity of the new correction for the data of $\alpha_{t,4} = 45°$

Though the regression of the sensible heat flux H with the data of $\alpha_{t,4} = 45°$ against that of SAT3 was improved by the new correction (Section 3.5.2), the frequency distribution results did not validate the new correction for this data (Section 3.5.1). Perhaps the mounting structure of the tilted SAT4 skewed the airflow, and the attack angle of the streamline became larger than horizontal. Note that the validity tests of Sections 3.5.1 and 3.5.2 were made by rotating the coordinate system of SAT4 on the fixed angle $\alpha_{t,4} = 45°$. Therefore, the planar fit method (Wilczak et al., 2001) was applied here, comparing the friction velocities u_* (m s^{-1}) of SAT3 ($\alpha_{t,3} = 0°$) and SAT4 ($\alpha_{t,4} = 45°$), before and after the new correction was applied.

The first rotation angles of the planar fit method for SAT4, before and after application of the new correction, were $-41.1°$ and $-48.0°$, respectively, representing the pitch angle about the v-axis (Wilczak et al., 2001). In contrast, the first rotation angles for SAT3 were almost unchanged—namely, $0.4°$ for uncorrected data and $0.5°$ for corrected data.

Fig. 13 is the scatter plot for u_* of SAT4 against that of SAT3. Before the correction was applied, u_* of SAT4 was larger than that of SAT3. After applying the new correction to the data, u_* values of SAT3 and SAT4 agreed well with one another, and the regression was also improved. This suggests that the raw data of the positive angle of attack was properly corrected by the new calibration
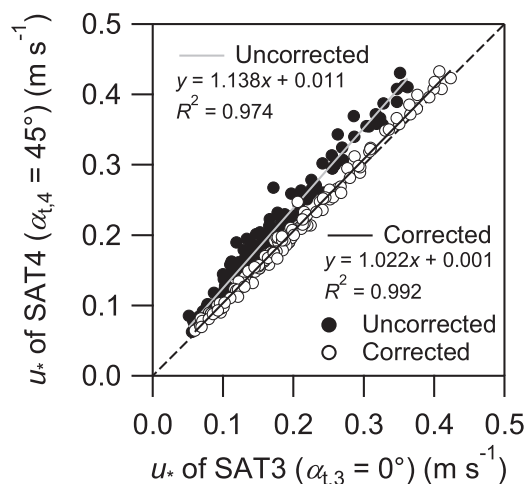

Fig. 13. Scatter plot of the friction velocity u_* (m s^{-1}) of SAT3 ($\alpha_{t,3} = 0°$) and of SAT4 ($\alpha_{t,4} = 45°$), before and after the application of the new correction.

functions, despite the fact that these functions were obtained for the data of the negative angle of attack only.

3.6. Effects of corrections on eddy fluxes

Fig. 14 shows the effect of corrections on the sensible heat flux H (Fig. 14(a)) and the latent heat flux λE (Fig. 14(b)). The results of the corrections of Nakai et al. (2006) and of this study are plotted. These fluxes were calculated using the data of SAT1 and KH-20, with both the double coordinate rotation (McMillen, 1988) and the humidity correction for sonic temperature (Schotanus et al., 1983) applied. These data were filtered by using the standard deviation of sonic temperature, $\sigma_T < 1.0$ K; standard deviation of water vapor concentration, $\sigma_q < 0.001$ kg m^{-3} (Nakai et al., 2006); and the ratio of the speed of the vector-averaged wind to the averaged instantaneous speed, $\sqrt{\overline{u}^2 + \overline{v}^2}/\overline{\sqrt{u^2 + v^2}} > 0.9$ (Vickers and Mahrt, 1997).

Applying the new correction, both H and λE were substantially increased. The flux increases due to the correction of this study were 14.2% in H and 13.9% in λE, even though they were observed over meadow, which is considered aerodynamically smooth compared to forests or agricultural fields. Note that these results were larger than the corrected results of Nakai et al. (2006). This suggests that the energy balance closure can be improved by correction of the angle of attack dependent errors, even over an aerodynamically smooth surface such as a short vegetation canopy. This could not be confirmed in this study, however, because the net radiation and soil heat flux were not measured during this observation.
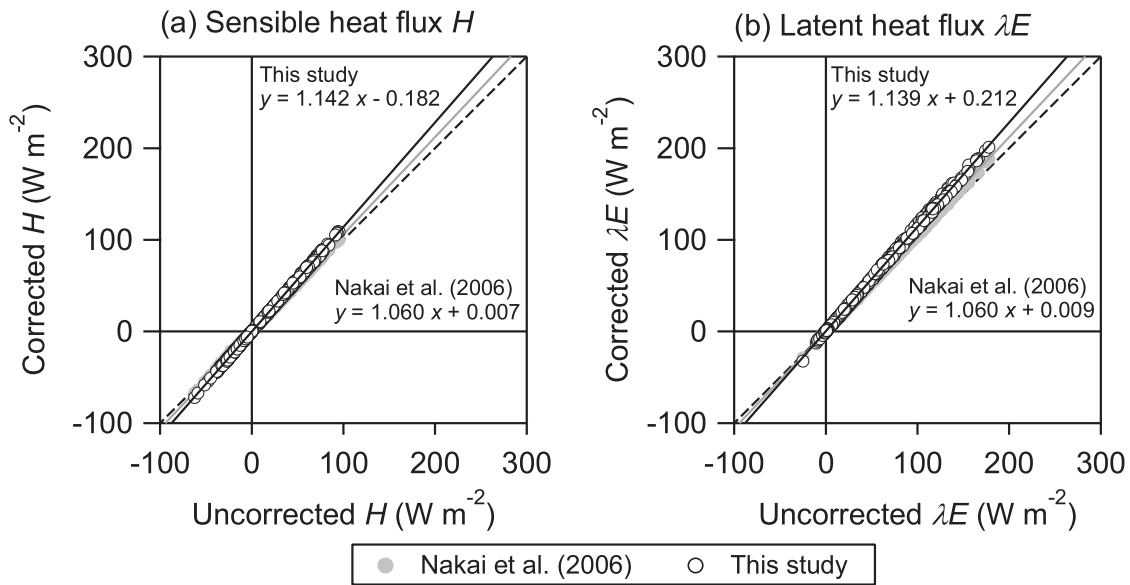
Fig. 14. Comparison of the effect of the corrections by Nakai et al. (2006) and this study upon (a) sensible heat flux H and (b) latent heat flux λE. The data of SAT1 and the KH20 krypton hygrometer were used.

4. Conclusion

Ultrasonic anemometer errors due to angle of attack under turbulent conditions were assessed carefully by the field experiment in the natural turbulent flow. The obtained results clearly showed that the angle of attack dependent errors occurred even under turbulent conditions. Observed sine and cosine responses differed somewhat from the previous calibration functions, representing the wind tunnel results. Adopting the new calibration functions to properly represent the observed data under turbulent conditions, the corrected sine and cosine responses were successfully restored to the $\sin\alpha$ and $\cos\alpha$, respectively. After application of the correction by the new calibration functions, the sensible and latent heat fluxes increased substantially, even though they were observed over meadow, which is considered aerodynamically smooth. Therefore, the correction of the angle of attack dependent errors will significantly affect the heat, water vapor, and carbon fluxes, not only over forests and agricultural fields but also over smooth surfaces such as grasslands, wetlands, and tundra bogs. Also, this correction can account for a large portion of the energy imbalance.

Appendix A. Coordinate system of the WindMaster and WindMaster Pro ultrasonic anemometers

This study and the source code of the new correction (see Appendix C) are based on the "X1 setting" coordinate system in Fig. A1, which is the instrument's default setting (Gill Instruments Ltd., 2009). Other omnidirectional ultrasonic anemometers by Gill
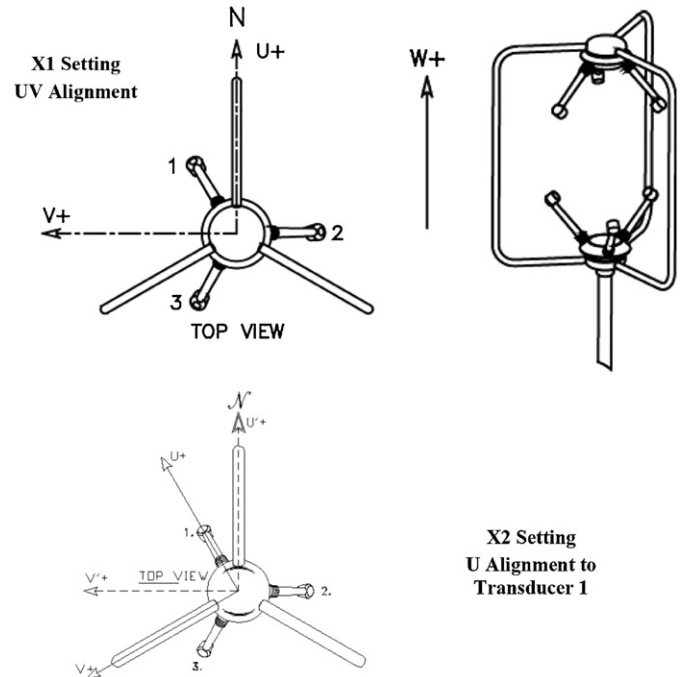

Fig. A1. Coordinate system of the WindMaster and WindMaster Pro ultrasonic anemometers.
From Gill Instruments Ltd., 2009.

Instruments with a shape identical to the WindMaster (Pro) have the same coordinate system and default setting, so this source code in Appendix C should be directly applicable. However, there is also an optional "X2 setting" setting, in which the U axis is aligned to the transducer 1. If this X2 setting is adopted, the rotated U' and V' are required when applying the correction (source code) of this study. These are calculated from the observed U and V as follows.

$$U' = U \cos 30° - V \sin 30°, \qquad (A.1)$$

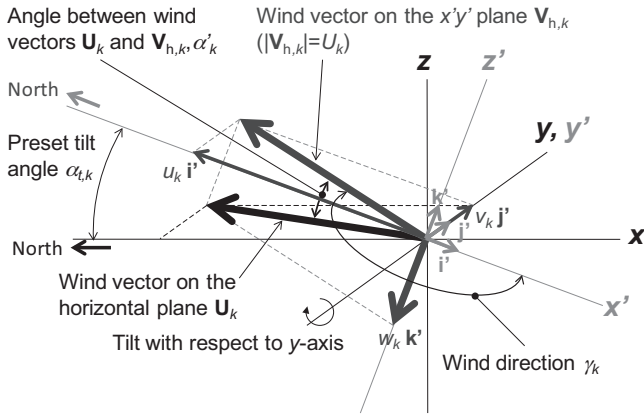$$V' = U \sin 30° + V \cos 30°. \qquad (A.2)$$

Fig. B1. Schematic diagram of Eq. (5), the relationship between preset tilt angle $\alpha_{t,k}$, wind direction γ_k, and angle α'_k between wind vector on the horizontal plane $\mathbf{U}_k$ and the horizontal plane of the tilted anemometer.

Appendix B. Derivation of Eq. (5)

Fig. B1 is a schematic diagram of Eq. (5), the relationship between preset tilt angle $\alpha_{t,k}$, wind direction γ_k, and angle α'_k. Let the normal coordinate system be the standard 3-dimensional Cartesian system (x, y, z), where x and y are the two horizontal coordinates and z is the vertical coordinate; and let the tilted coordinate system (x', y', z') be tilted with respect to the y-axis (therefore y-axis and y'-axis are the same). Let $\mathbf{i}'$, $\mathbf{j}'$, and $\mathbf{k}'$ denote unit vectors on the x'-axis, y'-axis, and z'-axis, respectively.

Let the given wind vector $\mathbf{U}_k$ be defined on the horizontal plane. $\mathbf{U}_k$ can be decomposed into the horizontal component on the $x'y'$ plane, $\mathbf{V}_{h,k}$ (where $|\mathbf{V}_{h,k}| = U_k$), and the vertical component w_k $\mathbf{k}'$ (z'-axis). $\mathbf{V}_{h,k}$ can also be decomposed into u_k $\mathbf{i}'$ (x'-axis) and v_k $\mathbf{j}'$ (y'-axis).

Wind direction γ_k is defined on the tilted $x'y'$ plane. Here, the angle between the wind vectors $\mathbf{U}_k$ and $\mathbf{V}_{h,k}$, α'_k, is not always equal to the preset tilt angle $\alpha_{t,k}$. In the case of $\gamma_k = 180°$, α'_k is equal to $\alpha_{t,k}$, and when $\gamma_k = 90°$ and $270°$, $\alpha'_k = 0°$. Note that the northern wind ($\gamma_k = 0°$) blows from north to south, and γ_k increases clockwise.

According to Fig. B1, the following equations can be derived:

$$w_k = U_k \tan \alpha'_k, \tag{B.1}$$

$$\frac{w_k}{u_k} = -\tan \alpha_{t,k}, \tag{B.2}$$

$$u_k = U_k \cos \gamma_k, \tag{B.3}$$

Substituting Eq. (B.3) into Eq. (B.2), the following equation is obtained:

$$w_k = -U_k \cos \gamma_k \cdot \tan \alpha_{t,k} \tag{B.4}$$

Therefore, substituting Eq. (B.1) into Eq. (B.4),

$$U_k \tan \alpha'_k = -U_k \cos \gamma_k \cdot \tan \alpha_{t,k},$$
$$\therefore \alpha'_k = \arctan(-\cos \gamma_k \cdot \tan \alpha_{t,k}). \tag{B.5}$$

Appendix C. Source code for the correction of angle of attack dependent errors with the new functions

The source code of C/C++ and other programming languages for the correction of angle of attack dependent errors with the new functions introduced in this study can be downloaded from the websites of Taro Nakai and the International Arctic Research Center Data Archive (IDA).

http://sites.google.com/site/micrometeorologist/ (Taro Nakai)
http://climate.iarc.uaf.edu/geonetwork/srv/en/main.home (IDA)

References

Cava, D., Contini, D., Donateo, A., Martano, P., 2008. Analysis of short term closure of the surface energy balance above short vegetation. Agric. For. Meteorol. 148, 82–93.

Foken, T., 2008. The energy balance closure problem: an overview. Ecol. Appl. 18, 1351–1367.

Gash, J.H.C., Dolman, A.J., 2003. Sonic anemometer (co)sine response and flux measurement. I. The potential for (co)sine error to affect sonic anemometer-based flux measurements. Agric. For. Meteorol. 119, 195–207.

Gill Instruments Ltd., 2009. WindMaster & WindMaster Pro Ultrasonic Anemometer User Manual. Saltmarsh Park, 67 Gosport Street, Lymington, Hampshire SO41 9EG, UK. Doc. No. 1561-PS-0001, Issue 04, 47 pp.

Högström, U., Smedman, A., 2004. Accuracy of sonic anemometers: laminar wind-tunnel calibrations compared to atmospheric in situ calibrations against a reference instrument. Boundary-Layer Meteorol. 111, 33–54.

McMillen, R.T., 1988. An eddy correlation technique with extended applicability to non-simple terrain. Boundary-Layer Meteorol. 43, 231–245.

Meyers, T., Heuer, M., 2006. A field methodology to evaluate sonic anemometer angle of attack errors. In: 27th Conference on Agricultural and Forest Meteorology, May 21–25, 2006, San Diego.

van der Molen, M.K., Gash, J.H.C., Elbers, J.A., 2004. Sonic anemometer (co)sine response and flux measurement. II. The effect of introducing an angle of attack dependent calibration. Agric. For. Meteorol. 122, 95–109.

Nakai, T., van der Molen, M.K., Gash, J.H.C., Kodama, Y., 2006. Correction of sonic anemometer angle of attack errors. Agric. For. Meteorol. 136, 19–30.

Schotanus, P., Nieuwstadt, F.T.M., DeBruin, H.A.R., 1983. Temperature measurement with a sonic anemometer and its application to heat and moisture fluctuations. Boundary-Layer Meteorol. 26, 81–93.

Twine, T.E., Kustas, W.P., Norman, J.M., Cook, D.R., Houser, P.R., Meyers, T.P., Prueger, J.H., Starks, P.J., Wesely, M.L., 2000. Correcting eddycovariance flux underestimates over a grassland. Agric. For. Meteorol. 103, 279–300.

Vickers, D., Mahrt, L., 1997. Quality control and flux sampling problems for tower and aircraft data. J. Atmos. Oceanic Technol. 14, 512–526.

Wilczak, J.M., Oncley, S.P., Stage, S.A., 2001. Sonic anemometer tilt correction algorithms. Boundary-Layer Meteorol. 99, 127–150.